Nano Energy 104 (2022) 107960

Contents lists available at ScienceDirect

Nano Energy

journal homepage: www.elsevier.com/locate/nanoen

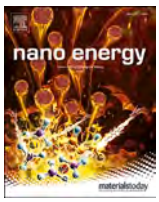

Highly active and stable amorphous IrO_x/CeO_2 nanowires for acidic oxygen evolution

Wangyan Gou [a,1], Zhaoming Xia [b,1], Xiaohe Tan [a], Qingyu Xue [a], Fan Ye [c], Sheng Dai [c], Mingkai Zhang [d], Rui Si [e], Yong Zou [a], Yuanyuan Ma [a,*], Johnny C. Ho [f,*], Yongquan Qu [a,*]

[a] Key Laboratory of Special Functional and Smart Polymer Materials of Ministry of Industry and Information Technology, School of Chemistry and Chemical Engineering, Northwestern Polytechnical University, Xi'an 710072, PR China
[b] Department of Chemistry, Tsinghua University, Beijing 100084, PR China
[c] State Key Laboratory of Chemical Engineering, East China University of Science and Technology, Shanghai 200237, PR China
[d] Frontier Institute of Science and Technology, Xi'an Jiaotong University, Xi'an 710049, PR China
[e] Zhangjiang Laboratory, Shanghai Synchrotron Radiation Facility, Shanghai 201204, PR China
[f] Department of Materials Science and Engineering, City University of Hong Kong, Kowloon, Hong Kong Special Administrative Region

ARTICLE INFO

Keywords:
Acidic oxygen evolution
Amorphous structure
Iridium oxide
Ceria
Electron buffer

ABSTRACT

Development of highly active and durable electrocatalysts for acidic oxygen evolution reaction (OER) remains an unresolved grand challenge. Here, we reported the amorphous IrO_x/CeO_2 nanowires as highly active and acid-stable OER catalysts through a facile electro-spinning/calcination approach. The amorphous catalysts delivered a high mass activity of 167 A g_{Ir}^{-1} at 1.51 V, a low overpotential of 220 mV at 10 mA cm^{-2}, and a stable performance for 300 h of continuous operation in acid. As revealed by complementary experimental and theoretical calculation results, the intimate nanoscale feature of IrO_x/CeO_2 creates abundant binary interfaces, at which CeO_2 as an electron buffer regulates the adsorption of oxygen intermediates, lowers the activation barrier of OER, and suppresses the over-oxidation and dissolution of Ir, thereby significantly enhancing the OER activity and stability. This work provides a new strategy for designing highly active and acid-resistant OER catalysts.

1. Introduction

The development of renewable energy relies heavily on energy conversion and storage technologies to mitigate the intermittency problems associated with wind and solar power. In addition to lithium-sulfur batteries, sodium-ion batteries, and metal-air batteries [1–4], electrocatalytic water oxidation, especially the oxygen evolution reaction (OER), plays a pivotal role in renewable energy production and storage technologies [5]. However, the state-of-the-art OER electrocatalysts are significantly limited by their relatively low efficiency and seriously unsatisfactory stability, which are predominantly ascribed to the catalytically sluggish OER kinetics and dynamically alternated physicochemical properties of the catalyst surfaces during operations, such as the alternated chemical compositions, (electro) chemical etching, aggregation, surface reconstruction, phase change, etc. [6–8]. Especially, the longevity of most OER electrocatalysts in acidic conditions is a grand challenge owing to the highly oxidizing and corrosively acidic operating environments. At the same time, the proton exchange membrane water electrolyzers exhibit many benefits for overall water splitting and show more promise for practical applications compared to the counterpart of alkaline electrolyzers [9–11]. Thus, developing efficient and stable water oxidation electrocatalysts in acidic media is challenging yet highly expected.

Many efforts have been placed on rationalizing acidic OER electrocatalysts with high activity and stability. To date, IrO_x, RuO_x, and their derivatives show the best OER catalytic performance in acidic media, in which Ir-based oxides show better stability but less activity than Ru-based oxides [12–14]. Extensive studies have been conducted to improve the acidic OER activity of Ir-based electrocatalysts by exposing more active sites and modulating the local electronic structures [15–20]. Despite those advances, both the life-time and activity of IrO_x as well as their derivatives, are still far from the expectation for practical applications. Although the deactivation mechanisms are still incomplete and under intense debate, the activity deterioration of Ir-based OER

* Corresponding authors.
E-mail addresses: yyma@nwpu.edu.cn (Y. Ma), johnnyho@cityu.edu.hk (J.C. Ho), yongquan@nwpu.edu.cn (Y. Qu).
[1] Wangyan Gou and Zhaoming Xia contributed equally to this work.

https://doi.org/10.1016/j.nanoen.2022.107960
Received 9 September 2022; Received in revised form 14 October 2022; Accepted 28 October 2022
Available online 1 November 2022

electrocatalysts can be generally attributed to the dissolution of iridium under the applied potentials in acidic electrolytes. The detailed deactivation mechanism investigations suggested that the formation of unstable Ir species induced the dominant Ir-dissolution under dynamic operating conditions, which were determined by the initial phases and structures of Ir-based electrocatalysts [21,22]. Among them, the amorphous IrO_x electrocatalysts exhibited improved activity due to the facile formation of reactive electrophilic O^{I-} oxygen species on the amorphous surface with the mixed-oxidation state of $Ir^{3+/4+}$ [23,24]. However, except for the in-situ electrooxidation of Ir metals, the facile methods for synthesizing amorphous iridium oxide are scarce. Moreover, continuous and gradual deactivation is still inevitable due to the transient reduction and oxidation between Ir^{4+} and Ir^{3+} as the predominant dissolution pathway for amorphous IrO_x electrocatalysts. Also, the formation of unstable $Ir^{>4+}$ leads to poor stability for amorphous IrO_x electrocatalysts and crystalline IrO_2 [25]. Even though the reasons for the dissolution of iridium-based catalysts are controversial, the consensus has been reached that aggressive change of oxidation states of interfacial iridium species leads to the dissolution of electrocatalysts. Inspired by these recognitions, integrating an electron buffer with IrO_x could be a feasible strategy to stabilize the oxidation states of iridium, which could theoretically minimize and even completely suppress the dissolution of iridium under the highly anodic and/or corrosive acidic OER environment.

CeO_2 with the reversible Ce^{3+}/Ce^{4+} redox pair has been widely introduced as an electronic promoter to modulate the local electronic structures of host electrocatalysts (e.g., IrO_x, Co_3O_4, metal phosphides, layered double hydroxide) and thereby enhance their performance for OER [26–29]. Most of those hybrid electrocatalysts for OER were performed in basic environments rather than in acidic electrolytes.

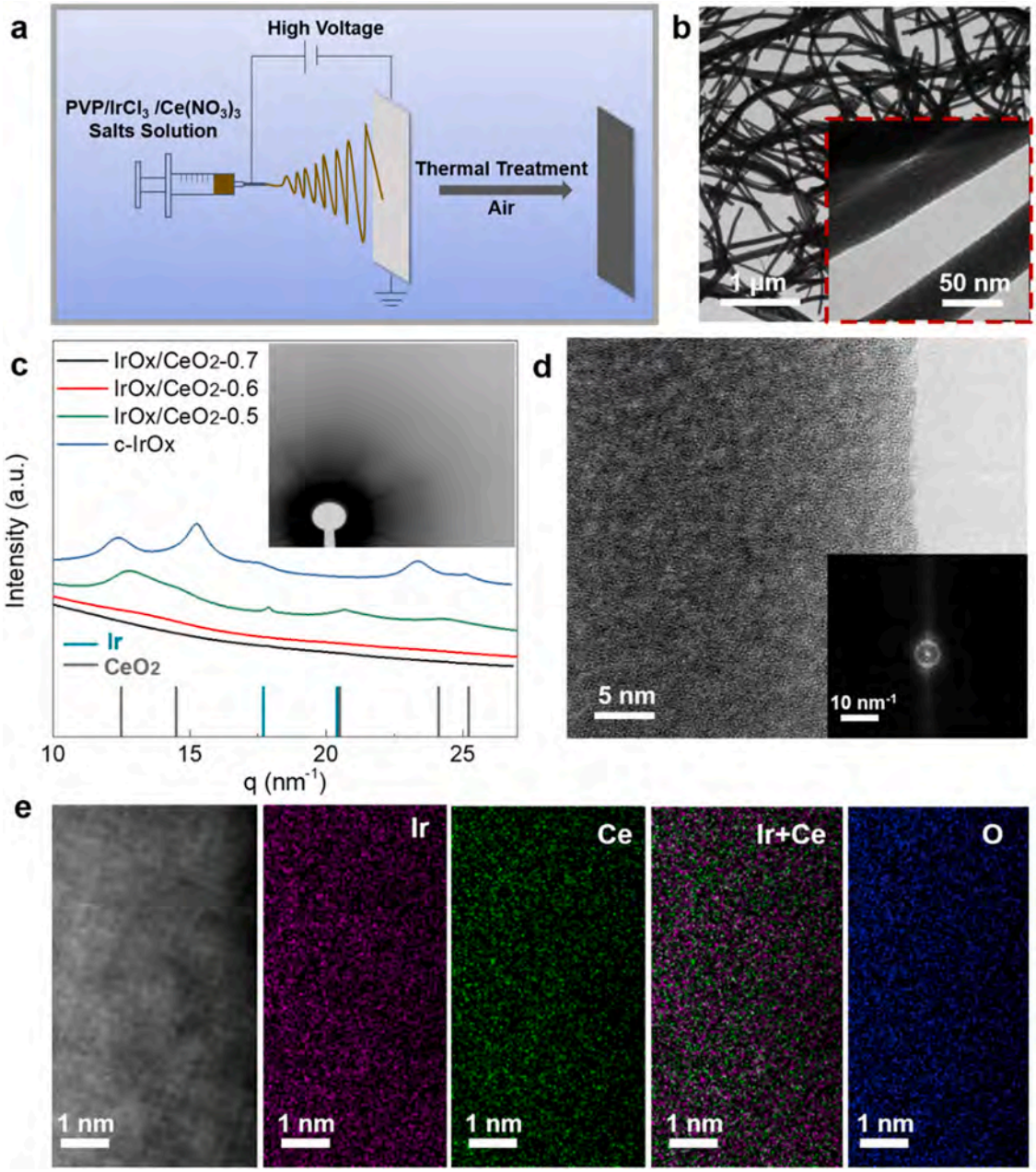

Fig. 1. Synthesis and characterizations. (a) Illustration of the synthetic procedure. (b) TEM images of IrO_x/CeO_2-0.6 nanowires. Inset shows the nanowire morphology with high-resolution and detail. (c) SAXS spectra of IrO_x/CeO_2-y and c-IrO_x. Inset shows the image plate of IrO_x/CeO_2-0.6. (d) HRTEM image of IrO_x/CeO_2-0.6. Inset shows the corresponding fast Fourier transform pattern. (e) The HAADF-STEM image and corresponding elemental maps of IrO_x/CeO_2-0.6.

Nevertheless, the integration of CeO_2 and IrO_x has not yet been explored for acidic OER. Motivated by those advances of CeO_2-incorporated electrocatalysts for basic OER and the high chemical stability of CeO_2 in acidic media, integrating CeO_2 and IrO_x and understanding CeO_2 as the electronic modulators on the local electronic structures of iridium species can provide a new approach to improve catalytic activity and stability of IrO_x for acidic OER.

Herein, using a facile electro-spinning synthesis methodology, we present highly active and stable amorphous IrO_x/CeO_2 nanowire electrocatalysts for water oxidation in 0.5 M H_2SO_4. The catalysts are featured by nanoscale intimacy and amorphous structure of the binary subnanometer-scale mixed IrO_x and CeO_2 particles in the nanowires, thereby providing abundant interfaces and favorable kinetics for acidic OER. In comparison with the commercially available IrO_x (c-IrO_x), the catalysts deliver a significantly high activity (220 mV of overpotential at 10 mA cm^{-2} and 167 A g_{Ir}^{-1} of mass activity) and a highly stable OER performance (> 300 h) in acid. Catalytic mechanism investigations illustrate that CeO_2 as an electron buffer not only enhances the catalytic activity of amorphous IrO_x but also lowers the Ir oxidation states during OER, thereby suppressing the iridium dissolution and ultimately exhibiting a highly active and robust performance for acidic OER.

2. Results and discussion

2.1. Synthesis and characterizations of amorphous IrO_x/CeO_2 nanowire

Amorphous IrO_x/CeO_2 nanowire electrocatalysts were prepared through a facile electro-spinning method from a sol precursor containing $IrCl_3$ and $Ce(NO_3)_3$ and sequential thermal treatments at high temperatures (Fig. 1a, see Experimental section in Supporting Information for details). The chemical compositions of the electrocatalysts were modulated by the initial molecular ratios of metal precursors. The electrocatalysts were named as IrO_x/CeO_2-y, where y represented the molar percentage of iridium. Initially, the morphology of electrocatalysts was examined by transmission electron microscopic (TEM, Fig. 1b and Fig. S1). The uniform wire-like morphology of the electrocatalysts with a diameter of ~50 nm and a length of several microns was observed as the molar ratios of Ir/Ce were larger than 1.0. When the molar proportion of Ce increased by over 50 %, the uniform nanowire morphology could not be maintained, accompanied by the irregular micron particles (Fig. S2). Structural features of the electrocatalysts were also characterized by small-angle X-ray scattering (SAXS, Fig. 1c) [30]. Comparing to the pronounced diffraction patterns of the commercial rutile c-IrO_x catalysts, no obvious diffraction peaks of IrO_x/CeO_2-0.7 and IrO_x/CeO_2-0.6 indicated the amorphous feature (Fig. S3), which was further confirmed by high-resolution TEM (HRTEM) images (Fig. 1d) and the selected area electron diffraction (SAED) patterns (inset of Fig. 1d) [31]. Meanwhile, the faint reflections of IrO_x/CeO_2-0.5 suggest a mixed phase of metallic

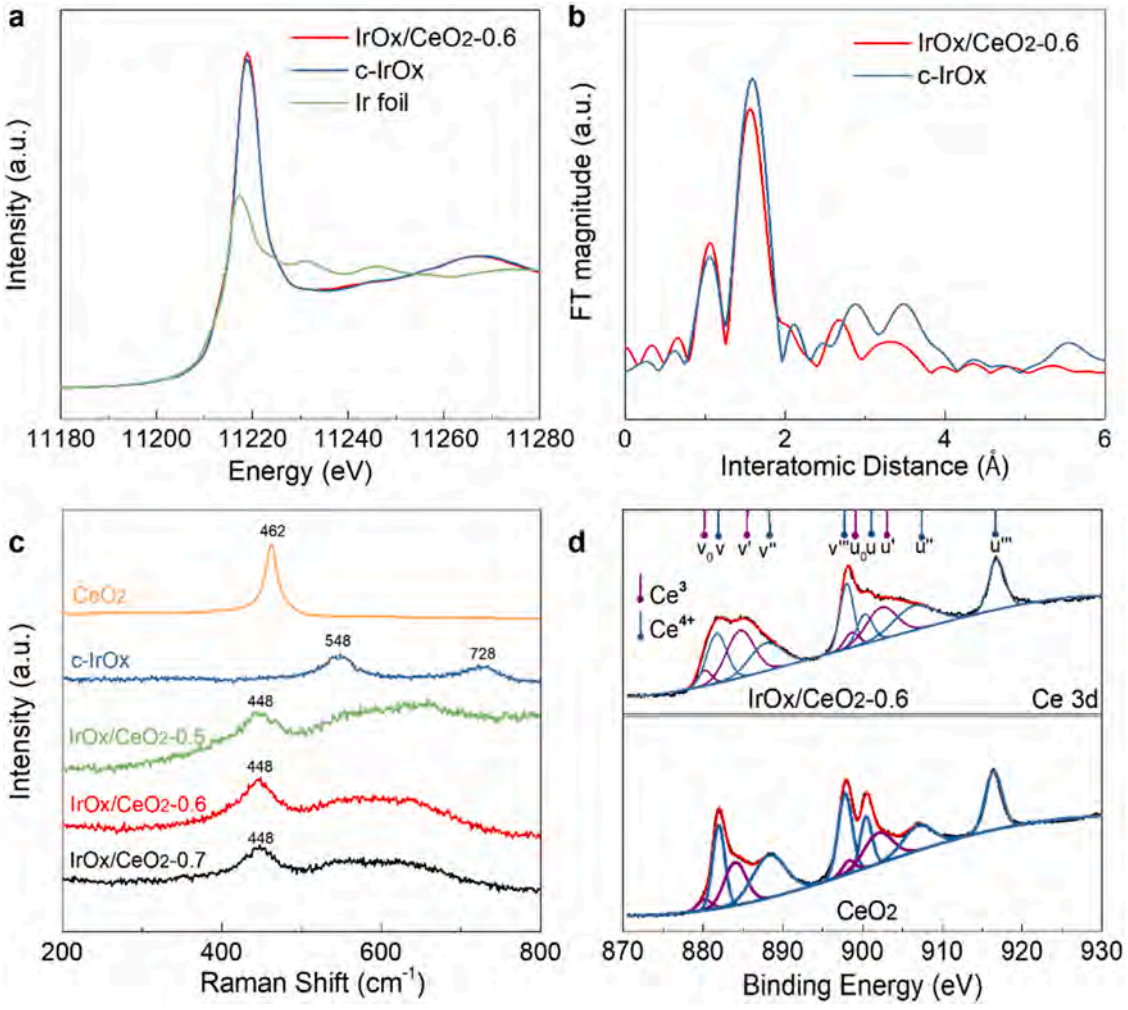

Fig. 2. X-ray adsorption and Raman spectra. (a) Iridium L-edge XANES spectra for IrO_x/CeO_2-0.6 and c-IrO_x. (b) EXAFS spectra for IrO_x/CeO_2-0.6 and c-IrO_x. (c) Raman spectra for IrO_x/CeO_2, c-IrO_x and CeO_2. (d) XPS spectra of Ce 3d for IrO_x/CeO_2-0.6 and CeO_2.

Ir and fluorite CeO_2. Through the control experiments, the suitable amount of cerium oxide (Fig. S4) and the appropriate calcination temperature (Fig. S5) guaranteed the formation of the amorphous structure. Energy-dispersive X-ray spectroscopy (EDS) elemental maps indicated the uniform distribution of iridium, cerium, and oxygen of IrO_x/-CeO_2-0.6 at the nanoscale (Fig. 1e). The EDS result (Fig. S6) further confirmed that the actual ratio of Ir and Ce of IrO_x/CeO_2-0.6 was 5.6:4.4, being close to the nominal ratios in the precursor mixtures.

2.2. Oxidation states of amorphous IrO_x/CeO_2 nanowires

The electronic and local geometrical structures of IrO_x/CeO_2-0.6 were characterized by X-ray absorption fine structure spectroscopy (XAFS), where the Ir foil and c-IrO_x catalysts were used as references. As shown in their X-ray absorption near edge structure (XANES) spectra (Fig. 2a), the Ir L_{III} edge spectra of IrO_x/CeO_2-0.6 displayed a similar spectral shape and edge position to that of c-IrO_x, indicating their nearly identical electronic structure in the bulk phase. Moreover, the extended X-ray absorption fine structure (EXAFS) spectra of IrO_x/CeO_2-0.6 and c-IrO_x showed the Ir-O contribution at a distance of 1.98 Å in the [IrO_6] octahedron (Fig. 2b), demonstrating the nearly identical Ir-O local geometrical structure between IrO_x/CeO_2-0.6 and c-IrO_x. The iridium coordination number of 5.3 of IrO_x/CeO_2-0.6 was slightly lower than that of bulk c-IrO_x (5.7), suggesting the smaller size of IrO_x in amorphous nanowires [31,32]. Raman spectroscopy was then conducted to explore the vibration of surface species on the electrocatalysts (Fig. 2c). Comparing to the Raman shift of Ce-O $F_{2\,g}$ vibration of the reference CeO_2 sample synthesized by the same electrospun method at 462 cm^{-1}, three IrO_x/CeO_2-y catalysts exhibited the significantly broadened and red shifted vibration peaks of Ce-O $F_{2\,g}$ at 448 cm^{-1}. It could be attributed to the fact that the amorphous structure is generally more disordered and has longer average cerium-oxygen bonds than the crystalline phase. This finding demonstrates the Ce–O coordination on the surface of amorphous catalysts showing a similar local structure to CeO_2 [33,34]. The c-IrO_x catalysts displayed the characterized Raman shifts of Ir-O vibrations at ~548 and 728 cm^{-1}. The broad Raman peaks of IrO_x/CeO_2-y from 510 cm^{-1} to 740 cm^{-1} were attributed to the two broadened peaks of Ir–O as well as one vibration peak of surface oxygen vacancies in CeO_2 (600 cm^{-1}) [35]. Taking all characterizations together, we can deduce that Ir and Ce species in the catalysts show a similar local structure with IrO_2 and CeO_2, respectively. Considering the uniform elemental distribution in Fig. 1, the bulk catalysts can be regarded as a uniform combination of IrO_2 and CeO_2 with nanoscale intimacy. The significant lattice mismatch between IrO_2 and CeO_2 grains results in an extremely-low-crystallinity state. Overall, the amorphous IrO_x/CeO_2 nanowires herein show the structural features of the nanoscale intimacy of binary components of IrO_x and CeO_2 with the spatial proximity, providing abundant interfaces of IrO_x/CeO_2 in electrocatalysts.

The oxidation states of Ir and Ce at the surface of the IrO_x/CeO_2-0.6 were analyzed by X-ray photoelectron spectroscopy (XPS). XPS spectra of Ir 4f (Fig. S7) suggest a similar mixture of Ir^{4+} and Ir^{3+} on the surfaces of both IrO_x/CeO_2-0.6 and c-IrO_x [36]. The surface trivalent and tetravalent cerium were monitored by deconvolution of Ce 3d core-level XPS spectra (Fig. 2d). The Ce 3d and O 1s (Fig. S8) spectra indicate a higher surface fraction of Ce^{3+} (37.4 %) associated with abundant oxygen vacancies on the surface of IrO_x/CeO_2-0.6, compared with the as-synthesized CeO_2 (Ce^{3+}%=24.3%) through the similar method [37,38]. Electron energy loss spectrum (EELS) also shows a mixture of Ce^{3+}/Ce^{4+} with a high-intensity ratio of M_5/M_4 peaks (Fig. S9), consistent with the XPS analysis [39,40]. Determined from ultraviolet photoelectron spectroscopy (UPS, Fig. S10), the position of the valence-band edge of the IrO_x/CeO_2-0.6 catalyst was about zero and near to E_f. Therefore, the IrO_x/CeO_2-0.6 catalysts showed the nearly same conducting properties as that of the commercial iridium oxide [41].

2.3. CeO_2 as an electron buffer

To experimentally explore the fundamental role of CeO_2, operando cyclic voltammetry (CV) was conducted to monitor the redox behavior of various catalysts. Throughout the continuous CV scanning, the position and currents of the redox peaks become stabilized. As shown in Fig. S11, the redox pair at 1.27 V (anodic) and 1.33 V (cathodic) was assigned to the deprotonation and re-protonation of the catalyst surface. The deprotonation/re-protonation process also affects Ir's oxidation states [42]. After that, we conducted a pH-dependence analysis of the cathodic peak on the IrO_x/CeO_2-0.6 and c-IrO_x catalysts in 0.5 M H_2SO_4 solution in the pH range of 0.36–1.26 (Fig. 3a and Fig. S12). The peak potentials vs. standard hydrogen electrode were plotted against the solution pH values. The slope of 198.3 ± 12.8 mV per pH unit of IrO_x/-CeO_2-0.6 suggests a $1e^-/3\,H^+$ coupled redox process, which is different from the 120 ± 3.0 mV per pH unit of c-IrO_x with a $1e^-/2\,H^+$ process (Fig. 3b) [43,44]. The pre-oxidation process can be described by the follow equations:

$$\left(\overset{+2x}{\text{Ir}}O_xH_y\Big/CeO_2\right)^{y+} = \left(\overset{+2x+0.33y}{\text{Ir}}O_x\Big/CeO_2\right)^{0.33y+} + yH^+ + 0.33ye^- \quad (1)$$

$$\left(\overset{+2x}{\text{Ir}}O_xH_y\right)^{y+} = \left(\overset{+2x+0.5y}{\text{Ir}}O_x\right)^{0.5y+} + yH^+ + 0.5ye^- \quad (2)$$

The averaged oxidation states are labeled at the top of Ir. Ir species in IrO_x/CeO_2 show a smaller increase of oxidation states compared to the IrO_x alone. Thus, we can make preliminary speculation that CeO_2 can act as an electron buffer to inhibit the over-oxidation of interfacial Ir species. In addition, CV curves of IrO_x/CeO_2-0.6 and c-IrO_x recorded at different scan rates in 0.5 M H_2SO_4 solution (Fig. S13) reveal the first-order power law relationship between the cathodic peak current densities and the scan rate (Fig. S14), suggesting that they are associated with a surface capacitive process [45].

Density functional theory (DFT) calculations were also conducted to examine the capability of CeO_2 as an electron buffer. The IrO_2/CeO_2 heterojunction model cannot be built by assembling of IrO_2 slab and CeO_2 slab because of their large lattice mismatch. To solve this problem, a Ce_3O_6-cluster was constructed on the IrO_2 (110) slab, followed by an ab initio molecular dynamics (AIMD) process. The detailed modeling methodology can be found in Fig. S15. The electronic capacitance properties were studied using a fix-potential method by JDFTx [46]. Assuming a quasi-equilibrium state in U_0 = 1.45 V vs. RHE, an equilibrium quantity of charge ($q_{1.45\,V}$) on the electrode will be spontaneously maintained to achieve an energy minimum of the system. Any charge disturbance ($q\text{-}q_{1.45\,V}$) of the electrode will lead to an energy increment, as shown in Fig. 3c. IrO_2/CeO_2 can hold or release electrons only at the cost of a smaller energy increment compared to pure IrO_2. With the assistance of CeO_2, the oxidation state of the surface Ir sites is stably maintained in a wide potential range (Fig. 3d). Therefore, CeO_2 is an electron buffer that stabilizes the oxidation state of Ir sites.

2.4. CeO_2 as an electron buffer for activity

To experimentally explore the fundamental catalytic properties of amorphous nanowires in the acidic electrolyte, we carried out a series of electrochemical measurements in 0.5 M H_2SO_4 solution by a three-electrode configuration with a graphite rod as the counter electrode and Ag/AgCl as the reference electrode. The catalyst loading for all electroactive materials was controlled at the total weight loading of 0.56 mg cm^{-2}. Initially, the electrocatalytic activity was evaluated by linear sweep voltammetry (LSV) method (Fig. 4a). The LSV curves of both IrO_x/CeO_2-0.6 and IrO_x/CeO_2-0.7 exhibited a sharp increased anodic current response starting at almost the same onset potential

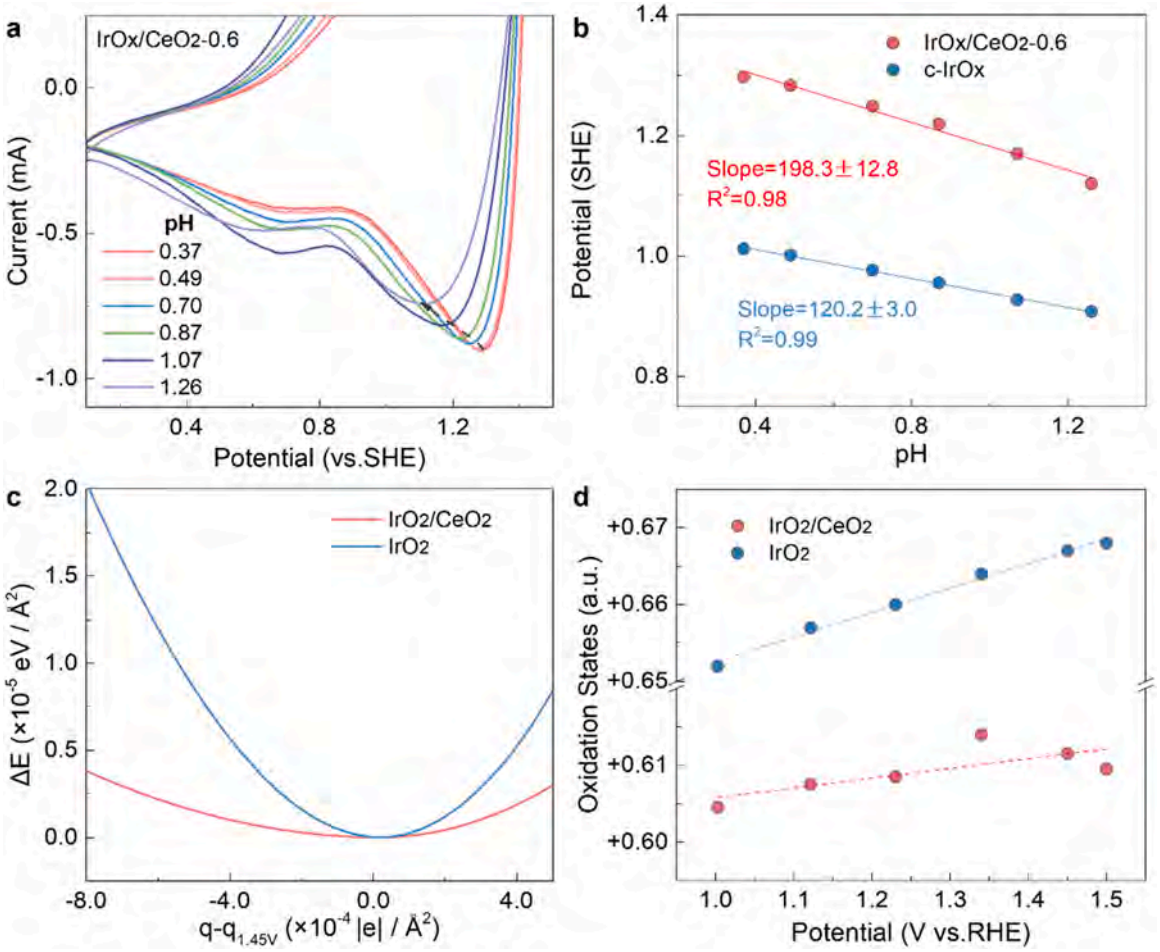

Fig. 3. The pH-dependence and oxidation state analysis of the catalysts. (a) CV curves of IrO_x/CeO_2-0.6 recorded in H_2SO_4 solutions with different pH values. (b) The plots of the cathodic peak potential vs. SHE plotted against the solution pH for IrOx/CeO_2-0.6 and c-IrO_x. (c) The energy cost for the electrode to hold or release extra charges. (d) The averaged oxidation states of surface Ir in different potentials, which were calculated according to the Lowdin population by the built-in algorithm in JDFTx.

(E_{onset}, the potential required to reach a specific current density of 0.1 mA cm^{-2}) of 1.37 V, indicating a greatly improved catalytic activity in comparison with other electrodes (E_{onset}=1.45 V for IrO_x/CeO_2-0.5, E_{onset}=1.46 V for c-IrO_x and E_{onset}=1.65 V for CeO_2). Due to the high Ir-loading in IrO_x/CeO_2-0.7 and slightly better catalytic performance of IrO_x/CeO_2-0.6, among various catalysts, IrO_x/CeO_2-0.6 was recognized as the best electrocatalysts to deliver the highest activity in the window of the applied potentials. The overpotential of IrO_x/CeO_2-0.6 for reaching 10 mA cm^{-2} (η_{10}) was 220 mV, which was much lower than those of IrO_x/CeO_2-0.5 (300 mV) and c-IrO_x (290 mV). The use of LSV curves to determine Tafel slope and exchange current density (J_0) provides insights into the catalytic kinetics of a given electrocatalyst, where the small Tafel slope and large J_0 generally suggest fast reaction kinetics. Notably, the IrO_x/CeO_2-0.6 catalysts exhibited the smallest Tafel slope of 63 mV dec^{-1} and the largest J_0 of 16.8 μA cm^{-2} at room temperature, compared with those of IrO_x/CeO_2-0.5 (Tafel slope=113 mV dec^{-1} and J_0 =12.6 μA cm^{-2}) and c-IrO_x (Tafel slope=78 mV dec^{-1} and J_0 =5.8 μA cm^{-2}). This observation suggests the significantly accelerated reaction kinetics in the rate-determined step and the higher electrocatalytic activity of amorphous IrO_x/CeO_2-0.6 nanowires for OER under the operating conditions (Fig. 4b). Also, IrO_x/CeO_2-0.6 gave out the highest Ir-mass activity of 167 A g_{IrOx}^{-1} at 1.51 V, which was 10.8 times higher than that of c-IrO_x under the same external potential (Fig. 4c and d). The electrochemical active area of each catalyst was measured by cyclic voltammetry (Fig. S16) and the intrinsic activity of each catalyst was also evaluated (Fig. S17). IrO_x/CeO_2-0.6 catalyst showed the highest intrinsic activity. The measured Faradaic efficiency of O_2 production from the IrO_x/CeO_2-0.6 catalyst was 97.4 %.

Interfacial charge transfer between electrocatalysts and absorbates is the essential step for electrocatalytic reactions. Operando electrochemical impedance spectroscopy (EIS), an effective method to identify charge transfer on the catalyst interface, was employed to analyze the structure-activity relationship and catalytic kinetics between the evolution of electrode surface species and OER. Fig. 4e and Fig. S18 illustrate the Bode plots of the measured impedance of the OER process on IrO_x/CeO_2-0.6 and c-IrO_x in 0.5 M H_2SO_4 solution from 1.10 V to 1.48 V. The corresponding Bode phase plots were fitted with an equivalent circuit (Fig. S20). The phase Peak **a** described by R_1 and CPE_1 in the high-frequency region (10^1-10^3 Hz) is caused by the surface-oxidation interface [47]. Unlike the barely changed R_1 of c-IrO_x, the resistance of R_1 of IrO_x/CeO_2-0.6 became smaller along with the increasing applied potentials, representing a potential-dependent electron transfer in the presence of CeO_2 (Fig. 4f). Beyond an applied potential of 1.35 V, the resistance of R_1 of IrO_x/CeO_2-0.6 became smaller than that of c-IrO_x, which could be attributed to the faster kinetics and more involved electrons on the surface-oxidation interface [48]. R_2 and CPE_2 between the frequency region 10^1-10^{-1} Hz represent the adsorption behavior of intermediates on the catalyst surface during the OER process. The R_2 of IrO_x/CeO_2-0.6 was lower than that of c-IrO_x beyond 1.40 V, demonstrating much faster kinetics in adsorbed intermediates during OER (Fig. S21a). The accumulation of reaction intermediates of IrO_x/CeO_2-0.6 derived from more than two times larger CPE_2 during the

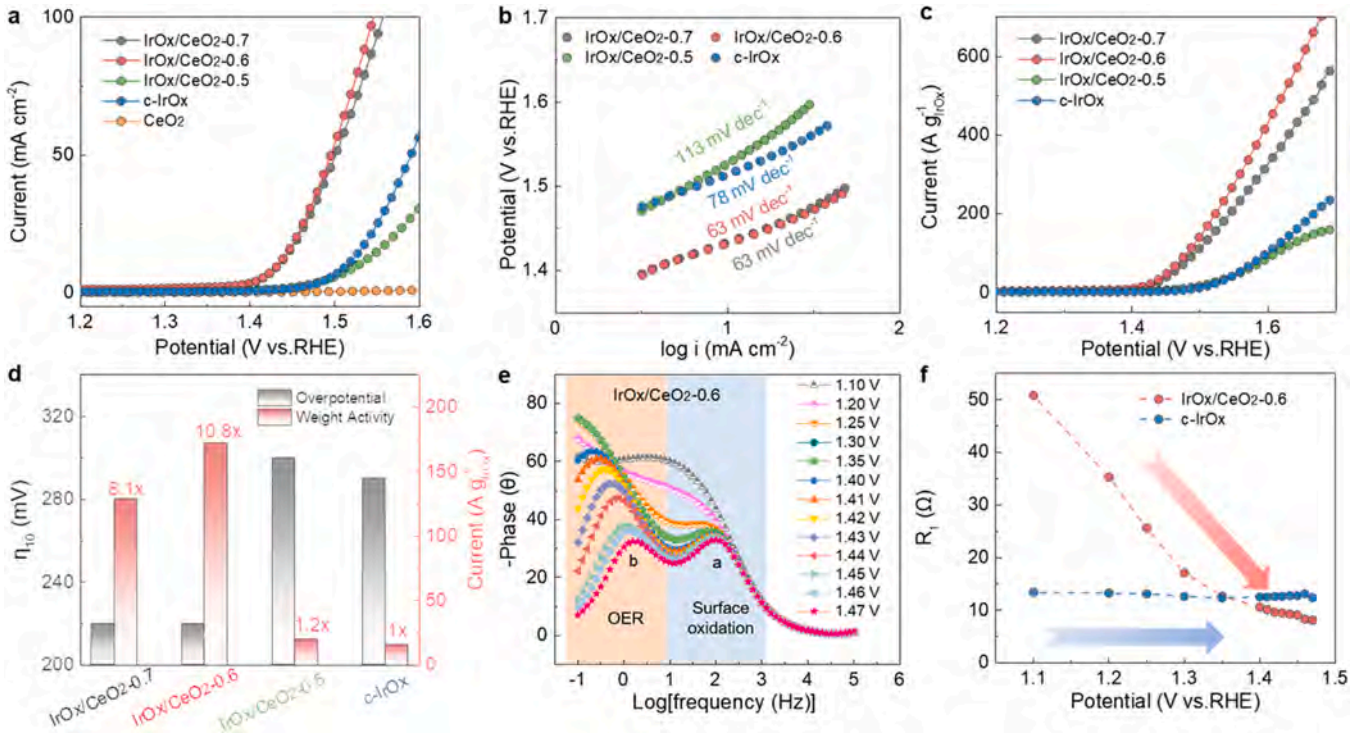

Fig. 4. Electrocatalytic OER performance. (a) LSV curves of various catalysts at a scanning rate of 10 mV s^{-1} in 0.5 M H_2SO_4. (b) Tafel plots for IrO_x/CeO_2-0.6 and c-IrO_x. (c) LSV curves of various catalysts normalized by unit mass of iridium oxide. (d) Comparison of overpotentials at a current density of 10 mA cm^{-2} and the normalized current densities based on a mass of iridium oxide at 1.51 V versus RHE. (e) Bode phase plots of IrOx/CeO_2-0.6. (f) Response of the R_1 charge transfer resistance to the applied potential of IrOx/CeO_2-0.6 and c-IrO_x.

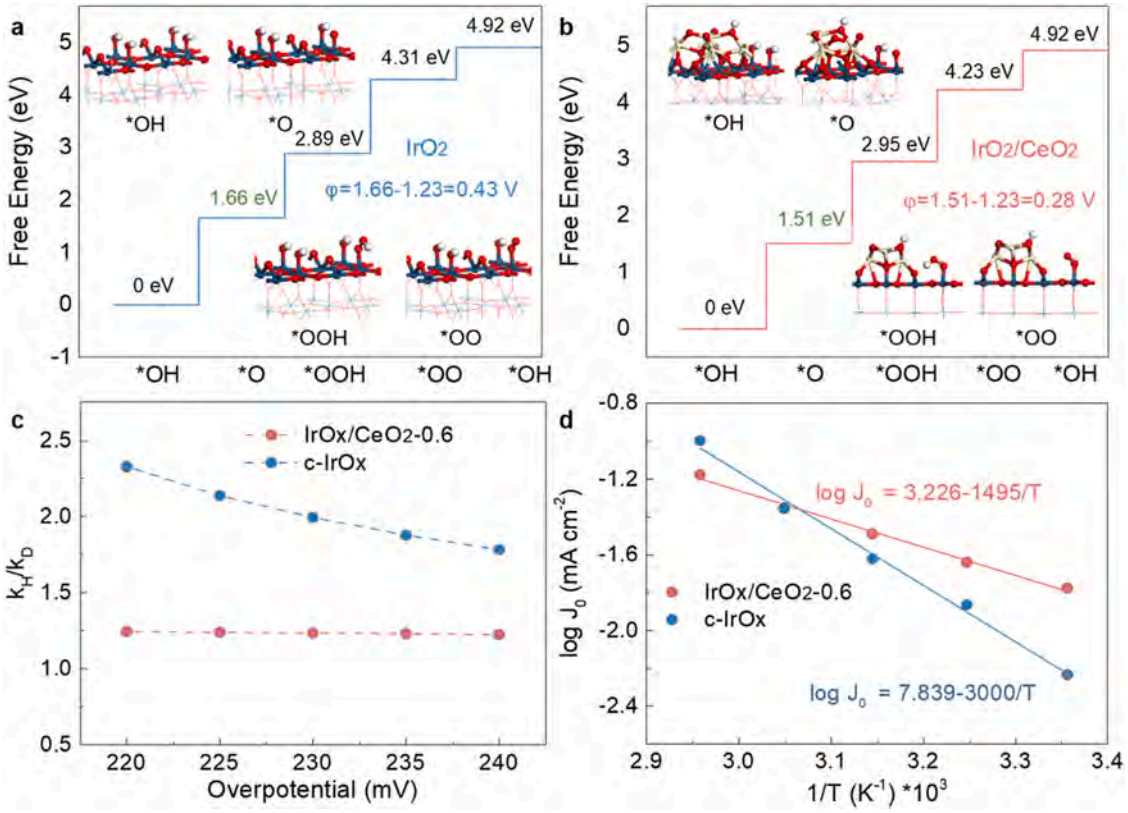

Fig. 5. DFT calculations, kinetic isotope effect (KIE), and activation energy analyses. (a) The free energy diagram and reaction pathways for OER on IrO_2. (b) The free energy diagram and reaction pathways for OER on IrO_2/CeO_2. (c) The calculated k_H/k_D values under different overpotentials. (d) Arrhenius plot of IrO_x/CeO_2-0.6 and c-IrO_x.

OER process could benefit the overall catalytic driving force (Fig. S21b) [49]. Overall, the charge-transfer resistance (R_{ct}=R_1 +R_2) of IrO_x/-CeO_2-0.6 was smaller than that of c-IrO_x, indicating that CeO_2 as the electron buffer facilitated electron transfer and intermediates adsorption and thus enhanced the intrinsic catalytic activity of IrO_x [50].

Theoretically, Ir sites in the simulated model covered with *OH have the lowest formation energy, and thus *OH is the intermediate with the highest coverage during the reaction (Fig. S22 and S23). *OH is the TOF-determining initial state (TDI) according to the energetic span model and thereby we consider *OH as the first intermediate of the reaction cycle [51]. The generation of every oxygen molecule requires four electrons, which can be divided into four electrochemical steps. 1) *OH → *O + H^+ + e^-; 2) *O + H_2O → *OOH + H^++ e^-; 3) *OOH→ *OO + H^+ + e^-; 4) *OO + H_2O → *OH + O_2 + H^++ e^-. The Gibbs free energy change of each step and the energy diagrams are shown in Fig. 5a and b. On both IrO_2 and IrO_2/CeO_2, the conversion of *OH to *O is the RDS. The calculated overpotential of IrO_2/CeO_2 is 0.28 V, much smaller than that of IrO_2 (0.43 V). This trend is highly consistent with the experimental results of the mass activity (Fig. 4c). Incorporation with CeO_2 modifies the intermediate adsorption energies and thus promotes the RDS to enhance catalytic performance.

To deepen the understanding of the mechanism, the Bader charge differences were calculated, which can be regarded as a descriptor of the oxidation states [52]. As shown in Fig. S24, the oxidation states of the active Ir site on IrO_2 show significant changes with different adsorption species. However, the oxidation states of the active Ir site on the IrO_2/CeO_2 surface are relatively less changed during the catalytic reaction. The IrO_2 model with *O species shows Ir's most positive oxidation states. In the case of the *O adsorbed on the IrO_2/CeO_2 model, most of the Ir-O bonds are longer than those of IrO_2 (Fig. S25). Bond length between metal and oxygen can influence the oxidation states of metal centers [53]. Herein, the longer Ir-O bonds weaken the interaction between Ir and O and hinder the electron transfer from Ir to O, preventing the active sites from over-oxidized. Besides the Ir–O bond length, the flexible Ce-O bonds are also crucial to regulating the oxidation state of Ir. CeO_2 with high oxygen mobility can significantly improve the flexibility of the Ir-O bond at the interface of IrO_x and CeO_2 [54]. As shown in Fig. S26, the Ce–O bond lengths show a wide distribution in the range of 2.05–2.90 Å, in which the long Ce-O bonds (> 2.35 Å) are mainly located at the CeO_2/IrO_2 interface. These long Ce–O bond lengths show a significant variation with the change of adsorbed species (Fig. S27). The Bader charge difference of Ir shows a strong correlation with the standard deviation of Ce–O bond length, indicating that oxygen species at the interface of CeO_2 and IrO_2 can make a massive surface relaxation turning into a disordered state if the local active sites are going to be over-oxidized. Consequently, the more disordered states exhibit a more flexible coordination pattern, which can effectively homogenize the oxidation states of surface species. Overall, CeO_2 serves as an electron buffer that regulates and controls Ir's oxidation states by surface relaxation during the OER reaction. This electron buffer prevented the Ir species in *O intermediates from being highly oxidative and highly-energetic Ir^{6+} state and reduced the energy barrier of OER.

The RDS kinetics and activation energy were verified afterward. To experimentally investigate the participation of H in the RDS, the H/D isotopic experiments were performed by using polarization curves sweeping to explore the roles of the CeO_2 in the OER process. Fig. S28 shows Tafel plots of IrO_x/CeO_2-0.6 and c-IrO_x measured in the acidic protium and deuterium solutions. Both catalysts exhibited parallel Tafel curves but slightly inferior OER current in KOD to that in KOH. The k_H/k_D value was further calculated to be in the range of 2.33–1.79 of c-IrO_x and was much higher than that of IrO_x/CeO_2-0.6 (1.22–1.25), representing a primary kinetic isotope effect (KIE) that involve H-related bond breaking event in the RDS (Fig. 5c) [55]. Thus, these results indicate that the CeO_2 play a vital role in facilitating the deprotonation process in the RDS, consistent with the DFT results. We extended the catalytic performance measurements of the IrO_x/CeO_2-0.6 and c-IrO_x catalysts at various temperatures, and the activation energy (E_a) was calculated by plotting the logarithmic values of exchange current density as a function of the inverse of the absolute temperatures (Fig. 5d and Fig. S29). According to the linear relationships, E_a was determined to be 28.6 kJ mol^{-1} for IrO_x/CeO_2-0.6 and 57.4 kJ mol^{-1} for c-IrO_x, respectively [56]. The much lower activation energy of the IrO_x/CeO_2-0.6 electrocatalysts suggests their considerably accelerated OER kinetics on the active interfacial sites, in accordance with the superior catalytic kinetics and DFT calculations of the binary amorphous nanowires in acid.

2.5. The electron buffer effect for stability

From the perspective of stability, it has been well documented that Ir with a high oxidation state can be easily dissolved into an acidic electrolyte. The electron buffer effect of CeO_2 suppresses the over-oxidation of the interfacial Ir species. It enables a relatively low oxidation state of Ir, which can greatly improve the stability of IrO_x theoretically. As expected, the IrO_x/CeO_2-0.6 electrocatalysts indeed delivered an impressively negligible decay of OER performance at 10 mA cm^{-2} after a 300 h of continuous operation in 0.5 M H_2SO_4 (Fig. 6a). Comparatively, the catalytic activity of c-IrO_x was quickly decayed during a period of 30 h, similar to the previous reports. The characterizations of the spent IrO_x/CeO_2-0.6 catalysts after stability test, including TEM, HRTEM, EDS, suggested the almost un-alternated structural features in IrO_x/CeO_2-0.6, demonstrating both structural robustness and catalytic stability (Fig. S30).

In order to further confirm the stabilized OER activity of IrO_x/CeO_2-0.6 due to the CeO_2 as the electron buffer and sequentially suppressed Ir dissolution, the inductively coupled plasma mass spectrometry (ICP-MS) measurements were conducted to monitor the electrolyte during chronoamperometric tests. The IrO_x/CeO_2-0.6 catalysts exhibited much low Ir dissolution rates of 0.78 %, 1.23 %, 1.56 %, 1.83 %, and 2.64 % of Ir at the time points of 1, 5, 10, 50 and 100 h of continuous operation, respectively, which outperformed the commercially available c-IrO_x as well as the majority of the previously reported Ir-based electrocatalysts

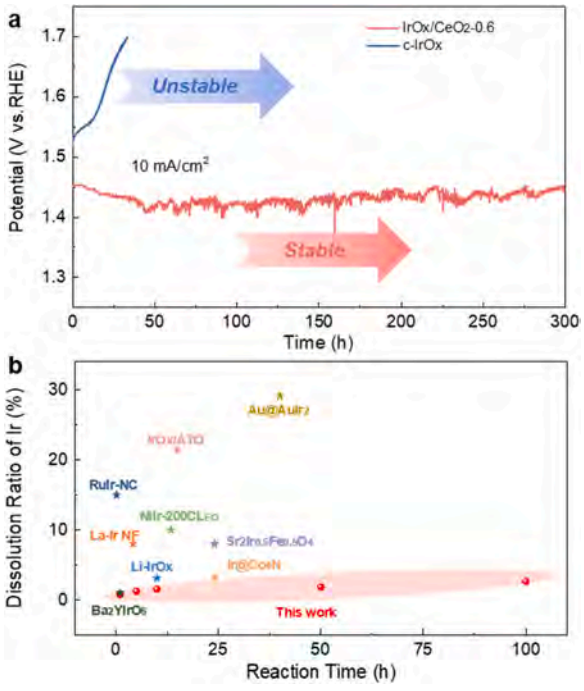

Fig. 6. OER stability. (a) Chronopotentiometry tests of IrO_x/CeO_2-0.6 and c-IrO_x at 10 mA cm^{-2}. (b) Comparison of the Ir dissolution in this work with the previous literatures.

(Fig. 6b) [21,31,57–63]. Also, ICP-MS results showed that the dissolution of Ir mainly occurred in the early stage and tended to be less in the later stage. The 7.5 % amount of Ce was dissoluted after 20 h-stability test, determined from ICP-MS. By examining XPS spectra of Ir before and after stability, the content of trivalent iridium slightly changed from 27.3 % of the initial catalysts to 25.2 % of the spent catalysts (20 h), indicating that the dissolution of Ce might not have a great influence on the surface state of Ir (Fig. S31). The activity of the catalyst was further improved after 20 h-stability test by examining the LSV curves (Fig. S32). By measuring the capacitance of the double layer, it could be concluded that cerium dissolution led to an increase in the electrochemical active area of the catalyst, which could be attributed to the more exposed active sites of Ir species (Fig. S33). Therefore, CeO_2 acts as an electron buffer agent inhibit Ir's dissolution and the electrochemical active area increases, which makes the IrO_x/CeO_2-0.6 catalysts highly stable.

3. Conclusion

In summary, we have developed a facile, scalable, and cost-effective method to prepare binary amorphous IrO_x/CeO_2 with nanoscale intimacy as the highly active and durable OER electrocatalysts throughout 300 h of continuous operation in acidic electrolyte. DFT calculations and control experiments demonstrate that CeO_2 serves as an electron buffer to accelerate the kinetics of the rate-determined step for the significantly enhanced activity and suppress the over-oxidation of Ir species as well as their dissolution for impressively promoted stability under practical conditions. Beyond the IrO_x/CeO_2 electrocatalysts illustrated herein, the strategy of introducing electron buffer can be applied to other acidic OER electrocatalysts, including RuO_x as well as other Ir-/Ru-compounds.

CRediT authorship contribution statement

W. Gou and Z. Xia contributed equally to this work. W. Gou carried out the experiments, collected and analyzed the experimental data. Z. Xia helped with the DFT calculations and assisted in the data analysis. X. Tan, Q. Xue, F. Ye, S. Dai, M. Zhang, R. Si, and Y. Zou participated in some of the experimental work. Y. Ma, J. C. Ho, and Y. Qu guided the project and contributed to the result analysis, discussion, and funding acquisition. W. Gou wrote the paper with feedback and guidance from Y. Ma, J. C. Ho, and Y. Qu. All authors discussed the results and commented on the manuscript at all stages.

Declaration of Competing Interest

The authors declare that they have no known competing financial interests or personal relationships that could have appeared to influence the work reported in this paper.

Data Availability

Data will be made available on request.

Acknowledgements

We acknowledge the National Nature Science Foundation of China (21872109). Y. Ma is supported by the National Natural Science Foundation of Shaanxi Province, China (No. 2020JM-039) and Fundamental Research Funds for the Central Universities (No. D5000210601). Y. Qu acknowledges the support from Fundamental Research Funds for the Central Universities (No. D5000210829). Z. Xia is supported by the China Postdoctoral Science Foundation (043260443). W. Gou is supported by the National Natural Science Foundation of Shaanxi Province, China (No. 2022JQ-433). The hard X-ray adsorption experiment (XANES and EXAFS) was performed at BL14W1 beam line in the Shanghai Synchrotron Radiation Facility (SSRF). The calculations were performed by using the HPC Platform at National Supercomputing Center in Tianjin. We thank H2 Cluster of Frontier Institute of Science and Technology, Xi'an Jiaotong University for supporting VASP resources in this study.

Appendix A. Supporting information

Supplementary data associated with this article can be found in the online version at doi:10.1016/j.nanoen.2022.107960.

References

[1] Y. Yan, P. Zhang, Z. Qu, M. Tong, S. Zhao, Z. Li, M. Liu, Z. Lin, Carbon/sulfur aerogel with adequate mesoporous channels as robust polysulfide confinement matrix for highly stable lithium-sulfur battery, Nano Lett. 20 (10) (2020) 7662–7669.
[2] M. Liu, P. Zhang, Z. Qu, Y. Yan, C. Lai, T. Liu, S. Zhang, Conductive carbon nanofiber interpenetrated graphene architecture for ultra-stable sodium ion battery, Nat. Commun. 10 (2019) 3917.
[3] Y. Yan, H. Cheng, Z. Qu, R. Yu, F. Liu, Q. Ma, S. Zhao, H. Hu, Y. Cheng, C. Yang, Z. Li, X. Wang, S. Hao, Y. Chen, M. Liu, J. Mater. Chem. A 9 (35) (2021) 19489–19507.
[4] Y. Yan, S. Liang, X. Wang, M. Zhang, S.-M. Hao, X. Cui, Z. Li, Z. Lin, Robust wrinkled MoS_2/N-C bifunctional electrocatalysts interfaced with single Fe atoms for wearable zinc-air batteries, PNAS 118 (40) (2021), e2110036118.
[5] Z.W. Seh, J. Kibsgaard, C.F. Dickens, I.B. Chorkendorff, J.K. Norskov, T. F. Jaramillo, Combining theory and experiment in electrocatalysis: insights into materials design, Science 355 (6321) (2017), eaad4998.
[6] L. An, C. Wei, M. Lu, H.W. Liu, Y.B. Chen, G.G. Scherer, A.C. Fisher, P.X. Xi, Z.C. J. Xu, C.-H. Yan, Recent development of oxygen evolution electrocatalysts in acidic environment, Adv. Mater. 33 (20) (2021), 2006328.
[7] H. Jin, B. Ruqia, Y. Park, H.J. Kim, H.S. Oh, S.I. Choi, K. Lee, Nanocatalyst design for long-term operation of proton/anion exchange membrane water electrolysis, Adv. Energy Mater. 11 (4) (2020), 2003188.
[8] F. Claudel, L. Dubau, G. Berthome, L. Sola-Hernandez, C. Beauger, L. Piccolo, F. Maillard, Degradation mechanisms of oxygen evolution reaction electrocatalysts: a combined identical-location transmission electron microscopy and X-ray photoelectron spectroscopy study, ACS Catal. 9 (5) (2019) 4688–4698.
[9] L.A. King, M.A. Hubert, C. Capuano, J. Manco, N. Danilovic, E. Valle, T. R. Hellstern, K. Ayers, T.F. Jaramillo, A non-precious metal hydrogen catalyst in a commercial polymer electrolyte membrane electrolyser, Nat. Nanotechnol. 14 (11) (2019) 1071–1074.
[10] C. Lin, J.L. Li, X.P. Li, S. Yang, W. Luo, Y.J. Zhang, S.-H. Kim, D.-H. Kim, S. S. Shinde, Y.F. Li, Z.-P. Liu, Z. Jiang, J.-H. Lee, In-situ reconstructed Ru atom array on alpha-MnO_2 with enhanced performance for acidic water oxidation, Nat. Catal. 4 (12) (2021) 1012–1023.
[11] Q. Yao, B. Huang, Y. Xu, L. Li, Q. Shao, X. Huang, A chemical etching strategy to improve and stabilize RuO_2-based nanoassemblies for acidic oxygen evolution, Nano Energy 84 (2021), 105909.
[12] C.C.L. McCrory, S. Jung, I.M. Ferrer, S.M. Chatman, J.C. Peters, T.F. Jaramillo, Benchmarking hydrogen evolving reaction and oxygen evolving reaction electrocatalysts for solar water splitting devices, J. Am. Chem. Soc. 137 (13) (2015) 4347–4357.
[13] T. Reier, M. Oezaslan, P. Strasser, Electrocatalytic oxygen evolution reaction (OER) on Ru, Ir, and Pt catalysts: a comparative study of nanoparticles and bulk materials, ACS Catal. 2 (8) (2012) 1765–1772.
[14] Y. Zhao, M. Luo, S. Chu, M. Peng, B. Liu, Q. Wu, P. Liu, F.M.F. de Groot, Y. Tan, 3D nanoporous iridium-based alloy microwires for efficient oxygen evolution in acidic media, Nano Energy 59 (2019) 146–153.
[15] Z. Pu, T. Liu, G. Zhang, H. Ranganathan, Z. Chen, S. Sun, Electrocatalytic oxygen evolution reaction in acidic conditions: recent progress and perspectives, ChemSusChem 14 (21) (2021) 4636–4657.
[16] L. She, G. Zhao, T. Ma, J. Chen, W. Sun, H. Pan, On the durability of iridium-based electrocatalysts toward the oxygen evolution reaction under acid environment, Adv. Funct. Mater. 32 (5) (2022), 2108465.
[17] S.Y. Hao, H.Y. Sheng, M. Liu, J.Z. Huang, G.K. Zheng, F. Zhang, X.N. Liu, Z.W. Su, J.J. Hu, Y. Qian, L.N. Zhou, Y. He, B. Song, L.C. Lei, X.W. Zhang, S. Jin, Torsion strained iridium oxide for efficient acidic water oxidation in proton exchange membrane electrolyzers, Nat. Nanotechnol. 16 (12) (2021) 1371–1377.
[18] L. Zu, X. Qian, S. Zhao, Q. Liang, Y.E. Chen, M. Liu, B.-J. Su, K.-H. Wu, L. Qu, L. Duan, H. Zhan, J.-Y. Zhang, C. Li, W. Li, J.Y. Juang, J. Zhu, D. Li, A. Yu, D. Zhao, Self-assembly of Ir-based nanosheets with ordered interlayer space for enhanced electrocatalytic water oxidation, J. Am. Chem. Soc. 144 (5) (2022) 2208–2217.
[19] H. Jin, S. Choi, G.J. Bang, T. Kwon, H.S. Kim, S.J. Lee, Y. Hong, D.W. Lee, H. S. Park, H. Baik, Y. Jung, S.J. Yoo, K. Lee, Safeguarding the RuO_2 phase against lattice oxygen oxidation during acidic water electrooxidation, Energy Environ. Sci. 15 (3) (2022) 1119–1130.
[20] X. Zhang, H. Su, X. Sun, C. Yang, Y. Li, H. Zhang, W. Zhou, M. Liu, W. Cheng, C. Wang, H. Wang, Q. Liu, Quick evolution of edge-shared metal-oxygen octahedrons for boosting acidic water oxidation, Nano Energy 102 (2022), 107680.

[21] R.H. Zhang, N. Dubouis, M. Ben Osman, W. Yin, M.T. Sougrati, D.A.D. Corte, D. Giaume, A. Grimaud, A dissolution/precipitation equilibrium on the surface of iridium-based perovskites controls their activity as oxygen evolution reaction catalysts in acidic media, Angew. Chem. Int. Ed. 58 (14) (2019) 4571–4575.
[22] C. Spöri, J.T.H. Kwan, A. Bonakdarpour, D.P. Wilkinson, P. Strasser, The stability challenges of oxygen evolving catalysts: towards a common fundamental understanding and mitigation of catalyst degradation, Angew. Chem. Int. Ed. 56 (22) (2017) 5994–6021.
[23] A. Grimaud, A. Demortiere, M. Saubanere, W. Dachraoui, M. Duchamp, M.-L. Doublet, J.-M. Tarascon, Activation of surface oxygen sites on an iridium-based model catalyst for the oxygen evolution reaction, Nat. Energy 2 (1) (2017) 16189.
[24] O. Kasian, S. Geiger, T. Li, J.-P. Grote, K. Schweinar, S. Zhang, C. Scheu, D. Raabe, S. Cherevko, B. Gault, K.J.J. Mayrhofer, Degradation of iridium oxides via oxygen evolution from the lattice: correlating atomic scale structure with reaction mechanisms, Energy Environ. Sci. 12 (12) (2019) 3548–3555.
[25] P. Jovanovič, N. Hodnik, F. Ruiz-Zepeda, I. Arcon, B. Jozinovic, M. Zorko, M. Bele, M. Sala, V.S. Selih, S. Hocevar, M. Gaberscek, Electrochemical dissolution of iridium and iridium oxide particles in acidic media: transmission electron microscopy, electrochemical flow cell coupled to inductively coupled plasma mass spectrometry, and X-ray absorption spectroscopy study, J. Am. Chem. Soc. 139 (36) (2017) 12837–12846.
[26] Q. Li, Z. Zeng, X. Sun, F. Luo, Y. Du, CeO_2 with diverse morphologies-supported IrO_x nanocatalysts for efficient oxygen evolution reaction-commemorating the 100th anniversary of the birth of academician Guangxian Xu, J. Rare Earths 39 (4) (2021) 357–363.
[27] B. Qiu, C. Wang, N. Zhang, L. Cai, Y. Xiong, Y. Chai, CeO_2-induced interfacial Co^{2+} octahedral sites and oxygen vacancies for water oxidation, ACS Catal. 9 (7) (2019) 6484–6490.
[28] M. Li, X. Pan, M. Jiang, Y. Zhang, Y. Tang, G. Fu, Interface engineering of oxygen-vacancy-rich CoP/CeO_2 heterostructure boosts oxygen evolution reaction, Chem. Eng. J. 395 (2020), 125160.
[29] Y. Li, X. Zhang, Z. Zheng, CeO_2 functionalized cobalt layered double hydroxide for efficient catalytic oxygen-evolving reaction, Small 18 (17) (2022), 2107594.
[30] E. Ortel, T. Reier, P. Strasser, R. Kraehnert, Mesoporous IrO_2 films templated by PEO-PB-PEO block-copolymers: self-assembly, crystallization behavior, and electrocatalytic performance, Chem. Mater. 23 (13) (2021) 3201–3209.
[31] J.J. Gao, C.-Q. Xu, S.-F. Hung, W. Liu, W.Z. Cai, Z.P. Zeng, C.M. Jia, H.M. Chen, H. Xiao, J. Li, Y.Q. Huang, B. Liu, Breaking long-range order in iridium oxide by alkali ion for efficient water oxidation, J. Am. Chem. Soc. 141 (7) (2019) 3014–3023.
[32] M. Elmaalouf, M. Odziomek, S. Duran, M. Gayrard, M. Bahri, C. Tard, A. Zitolo, B. Lassalle-Kaiser, J.-Y. Piquemal, O. Ersen, C. Boissiere, C. Sanchez, M. Giraud, M. Faustini, J. Peron, The origin of the high electrochemical activity of pseudo-amorphous iridium oxides, Nat. Commun. 12 (1) (2021) 3935.
[33] P. Simons, K.P. Torres, J.L.M. Rupp, Deposition parameters and Raman crystal orientation measurements of ceria thin films deposited by spray pyrolysis, J. Mater. Chem. A 10 (16) (2022) 8898–8910.
[34] M. Lykaki, E. Pachatouridou, S.A.C. Carabineiro, E. Iliopoulou, C. Andriopoulou, N. Kallithrakas-Kontos, S. Boghosian, M. Konsolakis, Ceria nanoparticles shape effects on the structural defects and surface chemistry: implications in CO oxidation by Cu/CeO_2 catalysts, Appl. Catal. B-Environ. 230 (2018) 18–28.
[35] A.V. Korotcov, Y.S. Huang, K.K. Tiong, D.S. Tsai, Raman scattering characterization of well-aligned RuO_2 and IrO_2 nanocrystals, J. Raman Spectrosc. 38 (6) (2007) 737–749.
[36] S.J. Freakley, J. Ruiz-Esquius, D.J. Morgan, The X-ray photoelectron spectra of IrO_2 and $IrCl_3$ revisited, Surf. Interface Anal. 49 (8) (2017) 794–799.
[37] C.-C. Shan, D.-S. Tsai, Y.-S. Huang, S.-H. Jian, C.-L. Cheng, Pt-Ir-IrO_2 NT thin-wall electrocatalysts derived from IrO_2 nanotubes and their catalytic activities in methanol oxidation, Chem. Mater. 19 (3) (2017) 424–431.
[38] L.L. Lin, S.Y. Yao, Z.Y. Liu, F. Zhang, N. Li, D. Vovchok, A. Martinez-Arias, R. Castaneda, J.Y. Lin, S.D. Senanayake, D. Su, D. Ma, J.A. Rodriguez, In situ characterization of Cu/CeO_2 nanocatalysts for CO_2 hydrogenation: morphological effects of nanostructured ceria on the catalytic activity, J. Phys. Chem. C 122 (24) (2018) 12934–12943.
[39] K.P. Song, H. Schmid, V. Srot, E. Gilardi, G. Gregori, K. Du, J. Maier, P.A. van Aken, Cerium reduction at the interface between ceria and yttria-stabilised zirconia and implications for interfacial oxygen non-stoichiometry, APL Mater. 2 (3) (2014), 032104.
[40] Y.Y. Li, W. Luo, D.J. Wu, Q. Wang, J. Yin, P.X. Xi, Y.Q. Qu, M. Gu, X.Y. Zhang, Z. G. Lu, Z.P. Zheng, Atomic-level correlation between the electrochemical performance of an oxygen-evolving catalyst and the effects of CeO_2 functionalization, Nano Res. 5 (2021) 2994–3000.
[41] R. Kötz, Ultraviolet photoelectron spectroscopy (UPS) of anodic oxide films on Au, Pt, Ru and $Ru_{0.5}1r_{0.5}$ alloy, Appl. Surf. Sci. 47 (2) (1991) 109–114.
[42] Z. Pavlovic, C. Ranjan, Q. Gao, M.V. Gastel, R. Schlögl, Probing the structure of a water-oxidizing anodic iridium oxide catalyst using Raman spectroscopy, ACS Catal. 6 (12) (2016) 8098–8105.
[43] J.Z. Huang, H.Y. Sheng, R.D. Ross, J.C. Han, X.J. Wang, B. Song, S. Jin, Modifying redox properties and local bonding of Co_3O_4 by CeO_2 enhances oxygen evolution catalysis in acid, Nat. Commun. 12 (1) (2021) 3036.
[44] M. Görlin, J.F. de Araujo, H. Schmies, D. Bernsmeier, S. Dresp, M. Gliech, Z. Jusys, P. Chernev, R. Kraehnert, H. Dau, P. Strasser, Tracking catalyst redox states and reaction dynamics in Ni-Fe oxyhydroxide oxygen evolution reaction electrocatalysts: the role of catalyst-support and electrolyte pH, J. Am. Chem. Soc. 139 (5) (2017) 2070–2082.
[45] T. Brezesinski, J. Wang, J. Polleux, B. Dunn, S.H. Tolbert, Templated nanocrystal-based porous TiO_2 films for next-generation electrochemical capacitors, J. Am. Chem. Soc. 131 (5) (2019) 1802–1809.
[46] S.A. Petrosyan, A.A. Rigos, T.A. Arias, Joint density-functional theory: ab initio study of Cr_2O_3 surface chemistry in solution, J. Phys. Chem. B 109 (32) (2005) 15436–15444.
[47] B. Zhou, Y.Y. Li, Y.Q. Zou, W. Chen, W. Zhou, M.L. Song, Y.J. Wu, Y.X. Lu, J.L. Liu, Y.Y. Wang, S.Y. Wang, Platinum modulates redox properties and 5-hydroxymethylfurfural adsorption kinetics of $Ni(OH)_2$ for biomass upgrading, Angew. Chem. Int. Ed. 60 (42) (2021) 22908–22914.
[48] D.J. Zhou, S.Y. Wang, Y. Jia, X.Y. Xiong, H.B. Yang, S. Liu, J.L. Tang, J.M. Zhang, D. Liu, L.R. Zheng, Y. Kuang, X.M. Sun, B. Liu, NiFe hydroxide lattice tensile strain: enhancement of adsorption of oxygenated intermediates for efficient water oxidation catalysis, Angew. Chem. Int. Ed. 58 (3) (2019) 736–740.
[49] Z.H. Xiao, Y.-C. Huang, C.-L. Dong, C. Xie, Z.J. Liu, S.Q. Du, W. Chen, D.F. Yan, L. Tao, Z.W. Shu, G.H. Zhang, H.G. Duan, Y.Y. Wang, Y.Q. Zou, R. Chen, S.Y. Wang, Operando identification of the dynamic behavior of oxygen vacancy-rich Co_3O_4 for oxygen evolution reaction, J. Am. Chem. Soc. 142 (28) (2020) 12087–12095.
[50] M.E.G. Lyons, M.P. Brandon, The significance of electrochemical impedance spectra recorded during active oxygen evolution for oxide covered Ni, Co and Fe electrodes in alkaline solution, J. Electroanal. Chem. 631 (1–2) (2009) 62–70.
[51] S. Kozuch, S. Shaik, How to conceptualize catalytic cycles? The energetic span model, Acc. Chem. Res. 44 (2) (2011) 101–110.
[52] W. Tang, E. Sanville, G. Henkelman, A grid-based Bader analysis algorithm without lattice bias, J. Phys.: Condens. Matter 21 (2009), 084204.
[53] N. Daelman, M. Capdevila-Cortada, N. López, Dynamic charge and oxidation state of Pt/CeO_2 single-atom catalysts, Nat. Mater. 18 (11) (2019) 1215–1221.
[54] J.L. Vincent, P.A. Crozier, Atomic level fluxional behavior and activity of CeO_2-supported Pt catalysts for CO oxidation, Nat. Commun. 12 (1) (2021) 5789.
[55] Y.M. Hao, Y.F. Li, J.X. Wu, L.S. Meng, J.L. Wang, C.L. Jia, T. Liu, X.J. Yang, Z.-P. Liu, M. Gong, Recognition of surface oxygen intermediates on NiFe oxyhydroxide oxygen-evolving catalysts by homogeneous oxidation reactivity, J. Am. Chem. Soc. 143 (3) (2021) 1493–1502.
[56] Y.F. Cheng, S.K. Lu, F. Liao, L.B. Liu, Y.Q. Li, M.W. Shao, Rh-MoS_2 nanocomposite catalysts with Pt-like activity for hydrogen evolution reaction, Adv. Funct. Mater. 27 (23) (2017), 1700359.
[57] S.-H. Cho, K.R. Yoon, K. Shin, J.-W. Jung, C. Kim, J.Y. Cheong, D.-Y. Youn, S. W. Song, G. Henkelman, I.-D. Kim, Synergistic coupling of metallic cobalt nitride nanofibers and IrO_x nanoparticle catalysts for stable oxygen evolution, Chem. Mater. 30 (17) (2018) 5941–5950.
[58] O. Diaz-Morales, S. Raaijman, R. Kortlever, P.J. Kooyman, T. Wezendonk, J. Gascon, W.T. Fu, M.T.M. Koper, Iridium-based double perovskites for efficient water oxidation in acid media, Nat. Commun. 7 (2016) 12363.
[59] W. Sun, C.L. Ma, X.L. Tian, J.J. Liao, J. Yang, C.J. Ge, W.W. Huang, An amorphous lanthanum-iridium solid solution with an open structure for efficient water splitting, J. Mater. Chem. A 8 (25) (2020) 12518–12525.
[60] F. Godínez-Salomon, L. Albiter, S.M. Alia, B.S. Pivovar, L.E. Camacho-Forero, P. B. Balbuena, R. Mendoza-Cruz, M.J. Arellano-Jimenez, C.P. Rhodes, Self-supported hydrous iridium-nickel oxide two-dimensional nanoframes for high activity oxygen evolution electrocatalysts, ACS Catal. 8 (11) (2018) 10498–10520.
[61] D.S. Wu, K. Kusada, S. Yoshioka, T. Yamamoto, T. Toriyama, S. Matsumura, Y. N. Chen, O. Seo, J. Kim, C. Song, S. Hiroi, O. Sakata, T. Ina, S. Kawaguchi, Y. Kubota, H. Kobayashi, H. Kitagawa, Efficient overall water splitting in acid with anisotropic metal nanosheets, Nat. Commun. 12 (1) (2021) 1145.
[62] H.-K. Oh, H.N. Nong, T. Reier, A. Bergmann, M. Gliech, J.F. de Araujo, E. Willinger, R. Schlogl, D. Teschner, P. Strasser, Electrochemical catalyst-support effects and their stabilizing role for IrO_x nanoparticle catalysts during the oxygen evolution reaction, J. Am. Chem. Soc. 138 (38) (2016) 12552–12563.
[63] H.M. Wang, Z.N. Chen, D.S. Wu, M.N. Cao, F.F. Sun, H. Zhang, H.H. You, W. Zhuang, R. Cao, Significantly enhanced overall water splitting performance by partial oxidation of Ir through Au modification in core-shell alloy structure, J. Am. Chem. Soc. 143 (12) (2021) 4639–4645.

Wangyan Gou received her Ph.D. degree from Frontier Institute of Science and Technology, Xi'an Jiaotong University in 2019. She received her Bachelor's degree from the School of Science, Xi'an Jiaotong University in 2014. She became a postdoctoral researcher in the School of Chemistry and Chemical Engineering, Northwestern Polytechnical University, in July 2020. Her research interest focuses on improving the activity and stability of electrocatalysts for oxygen evolution reaction, oxygen reduction reaction and hydrogen evolution reaction.

Zhaoming Xia received his Ph.D. from the Xi'an Jiaotong University, China, at 2019. He became a post-doctoral researcher in the department of chemistry in Tsinghua University from 2019 to 2022. His research is focused on the computational chemistry in areas of electrochemical catalysis and heterogeneous catalysis.

Xiaohe Tan received her BS degree from Qingdao University in 2021. She is currently working on her Master degree at Northwestern Polytechnical University under the supervision of Professor Yongquan Qu. Her research is focused on the electrocatalytic water splitting.

Qingyu Xue received his Bachelor's degree from the Yunnan University, China, at 2019, and he received his master's degree from the Xi'an Jiaotong University, China, at 2022. His research is focused on areas of heterogeneous catalysis in the electrocatalytic conversion of small organic molecules.

Fan Ye received her Ph.D. from the Xi'an Jiaotong University, China, at 2021, and worked as a post-doctoral researcher in the East China University of Science and Technology. Her research is focused on the mechanism of martensitic transformation.

Sheng Dai is a professor at School of Chemistry, East China University of Science and Technology in Shanghai, China. He received his B.E. and Ph.D. from Tsinghua University before completing postdoctoral training at the University of Michigan in Michigan and the University of California-Irvine. His research interest is focused on the use of in situ transmission electron microscopy to uncover the structure-property relationships of advanced catalysts.

Mingkai Zhang is a doctoral candidate in the Center for Applied Chemical Research at the Frontier Institute of Science and Technology, Xi'an Jiaotong University, China. He received his BS degree in chemical and biological engineering from Zhejiang University, China, and his MS degree in chemical engineering from Carnegie Mellon University. His research focuses on the activation of small molecules in heterogeneous catalysis.

Rui Si is currently a professor at School of Materials, Sun Yet-sen University. He received his BS in Materials Chemistry from Peking University in 2001, and PhD in Inorganic Chemistry from Peking University in 2006. He worked as a postdoctoral research fellow in Tufts University from 2006 to 2009 and Brookhaven National Laboratory (BNL) from 2009 to 2012. He joined in Shanghai Synchrotron Radiation Facility (SSRF) from 2013 to 2020 and moved to Sun Yet-sen University in 2020. His research interests focus on heterogeneous catalysis in operando characterization on supported catalysts.

Yong Zou received his Ph.D. from Xi'an Jiaotong University. He became a post-doctoral researcher in the School of Chemistry and Chemical Engineering, Northwestern Polytechnical University, in July 2022. His research interests focus on heterogeneous catalysis in the areas of organic catalysis including selective oxidation and CO_2 conversion to valuable chemicals.

Yuanyuan Ma is currently a professor at the School of Chemistry and Chemical Engineering, Northwestern Polytechnical University. She received his PhD degree from the University of California, Davis. Her current research focuses on the design of highly performed electrocatalysts for water splitting and organic transformations as well as the reaction mechanisms for electrochemical reactions.

Johnny Ho is currently a professor of Materials Science and Engineering at the City University of Hong Kong. He received his B. S. degree in chemical engineering and his M.S. and Ph.D. degrees in materials science and engineering from the University of California, Berkeley, in 2002, 2005, and 2009, respectively. From 2009–2010, he was a postdoctoral research fellow in the Nanoscale Synthesis and Characterization Group at Lawrence Livermore National Laboratory. His research interests focus on synthesis, characterization, integration, and device applications of nanoscale materials for various technological applications, including nanoelectronics, sensors, and energy harvesting.

Yongquan Qu is currently a professor at the School of Chemistry and Chemical Engineering, Northwestern Polytechnical University. He received his BS in Materials Science and Engineering from Nanjing University in 2001, MS in Chemistry from the Dalian Institute of Chemical Physics in 2004, and PhD in Chemistry from the University of California, Davis, in 2009. He worked as a postdoctoral research fellow in the University of California, Los Angeles, from 2009 to 2011. His research interests focus on heterogeneous catalysis in the areas of organic synthesis, clean energy production and biomimetic catalysis.